NANO EXPRESS

Study on Resistance Switching Properties of Na$_{0.5}$Bi$_{0.5}$TiO$_3$ Thin Films Using Impedance Spectroscopy

Ting Zhang · Xinan Zhang · Linghong Ding ·
Weifeng Zhang

Abstract The Na$_{0.5}$Bi$_{0.5}$TiO$_3$ (NBT) thin films sandwiched between Au electrodes and fluorine-doped tin oxide (FTO) conducting glass were deposited using a sol–gel method. Based on electrochemical workstation measurements, reproducible resistance switching characteristics and negative differential resistances were obtained at room temperature. A local impedance spectroscopy measurement of Au/NBT was performed to reveal the interface-related electrical characteristics. The DC-bias-dependent impedance spectra suggested the occurrence of charge and mass transfer at the interface of the Au/NBT/FTO device. It was proposed that the first and the second ionization of oxygen vacancies are responsible for the conduction in the low- and high-resistance states, respectively. The experimental results showed high potential for nonvolatile memory applications in NBT thin films.

Keywords Na$_{0.5}$Bi$_{0.5}$TiO$_3$ (NBT) thin films · Resistance switching · Impedance spectroscopy · Interfacial characteristics · Oxygen vacancies

Introduction

Reversible resistance switching (RS) in oxide thin films has recently attracted great interest in semiconductor industry due to the potential for using these films to make a new type of nonvolatile memories, which is often called resistance random access memory (RRAM) [1]. The RRAM has the superior properties of good retention, high endurance, rapid operation, low-power consumption, and especially due to its three-dimensional multistack structure that enables it to realize ultrahigh density memory [2]. Because of excellent RS effect, a number of perovskite metal oxides, such as SrTiO$_3$, [3] La$_{0.7}$Ca$_{0.3}$MnO$_3$, [3, 4] PbZr$_{0.2}$Ti$_{0.8}$O$_3$, [3, 5] (Ba, Sr) (Zr, Ti)O$_3$, [3, 6] and Pr$_{0.7}$Ca$_{0.3}$MnO$_3$ [7] have been studied extensively. To explain the intriguing effect, numerous theoretical models have been proposed. However, most of these models leave unanswered questions [8–10]. Despite its fundamental importance, our understanding of the underlying physics of the RS effect is still poor. The microscopic origin of the RRAM in perovskite metal oxides is not understood clearly.

Sodium bismuth titanate Na$_{0.5}$Bi$_{0.5}$TiO$_3$ (NBT) with perovskite structure is the best known lead-free piezoelectric and ferroelectric material that promises a number of applications in sensors and actuators since the first report on its ferroelectricity by Smolenskii et al. [11]. However, NBT in thin film form has not been properly investigated although NBT in bulk ceramic form has been widely studied [12]. Moreover, the resistive switching properties of the NBT thin films were less studied up to date. In this work, we discovered that reversible resistive switching occurs repeatedly at room temperature in a NBT thin films simply layered between the top and bottom electrodes. Therefore, this study may lead to a better understanding of perovskite-based memory device for nonvolatile memory (NVM) applications.

Experimental

(Na$_{0.5}$Bi$_{0.5}$)TiO$_3$ (NBT) thin films were prepared on fluorine-doped tin oxide (FTO) conducting glass substrates via

T. Zhang · X. Zhang · L. Ding · W. Zhang (✉)
Key Laboratory of Photovoltaic Materials of Henan Province,
School of Physics and Electronics, He'nan University, 475004
Kaifeng, People's Republic of China
e-mail: wfzhang@henu.edu.cn; wfzhang6@163.com

T. Zhang
e-mail: tingtingzhang2005@163.com

a sol–gel method with spin-coating process. Bismuth nitrate [Bi(NO$_3$)$_3$·5H$_2$O], sodium acetate [Na(CH$_3$COO)], and titanium butoxide [Ti(OC$_4$H$_9$)$_4$] were used as the starting materials. 2-methoxyethanol and glacial acetic acid were selected as the solvent and pH value adjusting reagent, respectively. To compensate for bismuth loss during the annealing treatment, 10% molar excess bismuth was added to the above mixture. The concentration of the final solution was adjusted to 0.3 M. The NBT coating solution was deposited onto FTO substrates by spin-coating at 3600 rpm for 30 s. After the spin-coating process, the specimen were heated-treated at 190 °C for 180 s to dry the wet gel films, then heated at 380 °C for 180 s to eliminate the organic groups, and finally annealed at 750 °C for 240 s. The thickness of only one deposition NBT films was calculated to be approximately 60 nm by four-layer sample on the observation under a JSM-5600 scanning electron microscope (SEM) in Fig. 1a. The surface morphology of the NBT films was measured by a SPA-400 atomic force microscope (AFM), and the results are presented in Fig. 1b. The film grown under 750 °C is rather smooth, and the grains are uniform. After deposition, a 20-nm-thick circular Au electrode with an area of 7.1×10^{-4} cm^2 was patterned through a metal mask to form sandwich structure by dc sputtering.

Cyclic voltammetry, multipotential steps, and A.C. impedance were undertaken on a CHI600B electrochemical workstation (Shanghai Chenhua, China). All the electrochemical measurements were carried out using
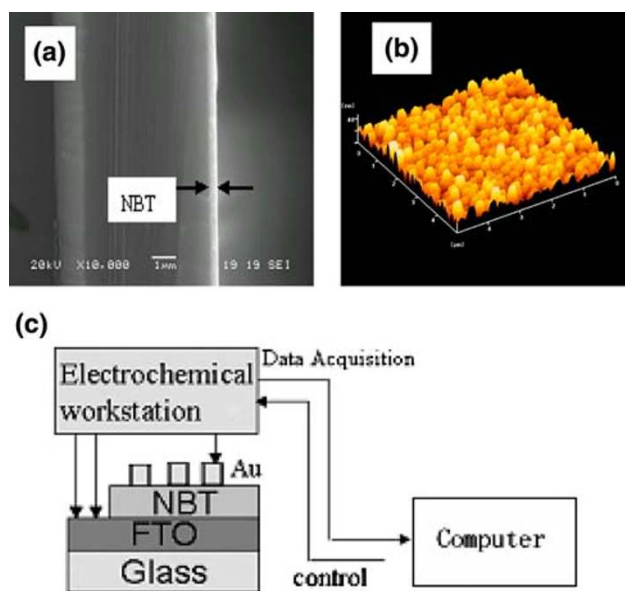
three-electrode system at room temperature, with FTO as reference electrode and counter electrode and Au as working electrode. The data were obtained using a computer-controlled program. A schematic drawing of the structure is shown in Fig. 1c.

Results and Discussion

The XRD patterns were collected on a DX-2500 X-ray diffractometer, employing Cu Ka radiation (1.542Å). From Fig. 2, the XRD study shows several peaks corresponding to NBT diffraction peaks accompanied by SnO$_2$ (FTO substrate) diffraction peaks, indicating that the films were single phased without any impurity.

To get a further knowledge about the colossal electroresistance (CER) effects in the Au/NBT/FTO system, we performed a careful study of the current–voltage (I–V) dependence. Figure 3 shows the I–V characteristics of Au/NBT/FTO sandwich structure for resistance switching. As can be seen from Fig. 3, when the bias is ramped from zero to the reset voltage, the sample exhibits a low-resistance state (LRS). Applying positive voltage, LRS could be changed to a high-resistance state (HRS). When the polarity of the bias is changed, the device switches to the LRS. Upon increasing the bias above the switching voltage, the device switches back to the HRS. Normally, peaks in I–V are attributed to a Faradaic reaction. Such peaks are the result of Maxwell-Boltzmann statistics governing electron transfer modified by the mass transport of the ions. It is interesting that the I–V curves never cross at the origin. It is not difficult to understand using the conducting domain model [13]. The qualitative form of the hysteresis depends on the intrasystem (top/center and bottom/center) charge transfers compared to the interface (top/electrode

Fig. 1 a Cross section of the sample obtained from four-layered deposition on the FTO conducting glass measured by SEM. b AFM image of the NBT thin films annealed at 750 °C. c Schematic diagram of I–V measurement system
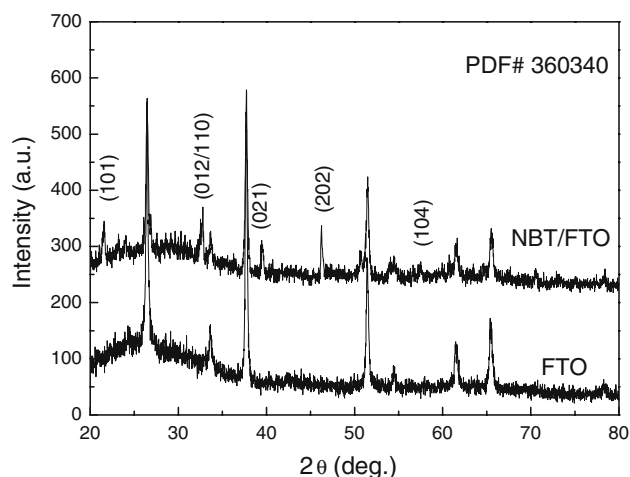

Fig. 2 XRD patterns of the NBT thin films on FTO conducting glass

and bottom/electrode) ones, both of which are controlled by the model parameters. When $\Gamma^{ext} \ll \Gamma^{int}$, where Γ^{ext} denotes the tunneling rates between the electrode and the top domains and Γ^{int} denotes the tunneling rates between the top domains and the central domains, the current shows low to high current switching. Assuming that larger interface transfers should be appropriate for high to low current switching systems, the hysteresis obtained in Au/NBT/FTO heterostructures qualitative agreement with the model was observed, as shown in Fig. 3. A distinctive negative differential resistance (NDR) appeared in the curves. Under increasing the scan rate, the peaks moved toward higher potential, but the NDR effect was consistently found in all measures. It was reported that the NDR is caused by the motion of oxygen ions at the $Ti/Pr_{0.7}Ca_{0.3}MnO_3$ interface [14]. It is possible that NBT has a similar effect because it is similar to PCMO in terms of octahedral crystal structure. In the inset of Fig. 3, 100 consecutive measurements were performed with a 0.05 V/s scanning rate between 6 and −6 V. The device shows a dipolar switching behavior and a good retention characteristic.

The domain model may simulate very divergent dc I–V characteristics by adjusting the fitting parameters [15], and the ac impedance is expected to investigate the resistance switching. Complex-impedance-plane plots are very popular because the shape of the locus of points yields insight into possible mechanisms or governing phenomena. If the locus of points traces a perfect semicircle, for example, the impedance response corresponds to a single activation energy-controlled process [13], where each data point corresponds to a different measurement frequency. Furthermore, the impedance spectrum may provide useful information to understand the charge transfer and mass transport that occurred at the interface. The bulk- and

interface-related properties could be effectively separated by using impedance spectroscopy.

The impedance spectra of the sample in the frequency range (100–100000 Hz) were measured at 1 V dc bias with voltage oscillation amplitude of 5 mV in Fig. 4a. Intentionally, before the measurement of impedance spectroscopy, the Au/NBT/FTO-assembled circuit was driven by a continuous sweeping voltage to first switch on and then terminate at the switching off state. The equivalent circuit at different electronic states can be described by a resistor R_e in series with the parallel combination of R and capacitor C synchronously, where one resistance is considered for the Ohmic resistance (R_e), and a net made of a surface capacitance of a film and electronic resistance of a semiconductor models the charge transfer of an electrochemical reaction at the electrode–semiconductor interface (RC activation time constant).

For a resistor R_e in series with the parallel combination of R and capacitor C, the impedance is given by [16]

$$Z = R_e + \frac{R}{1 + j\omega RC} \tag{1}$$

or

$$Z = R_e + \frac{R}{1 + (\omega RC)^2} - j\frac{\omega CR^2}{1 + (\omega RC)^2} \tag{2}$$

For low frequencies, the total resistance equals the sum of R_e and R. With increasing frequencies, the impedance of the capacitance will reduce. At very high frequencies, the impedance of the capacitance is almost zero and therefore acts as a short circuit. Thus, R_e is directly measured at high frequencies. A characteristic angular frequency $\omega_{RC} = 1/(RC)$ can be identified for which the imaginary part of the impedance has a maximum value $R/2$.

In Fig. 4a, whole semicircle cannot be obtained at room temperature due to the measurements at high frequency beyond the frequency range of our equipment. The impedance spectra characteristics of on and off states exhibit a high resistive value. As well known, sol–gel method is relatively vulnerable to surface contamination and other byproduct impurities. So a high density of defects exists at the Au/NBT interface, where the high density of surface states induced by the defects may cause a large degree of band bending and then influence the validity of the metal/semiconductor contact rule in our Au/NBT/FTO heterostructures. The high resistive region may stem from the Au/NBT interface due to the oxygen diffusion from the NBT film into the Au electrode, thus leaving a thin oxygen depletion layer at the Ag/NBT interface. It is well known that in the titanate-based perovskite oxides, the ionization of the oxygen vacancies will create the conducting electrons,
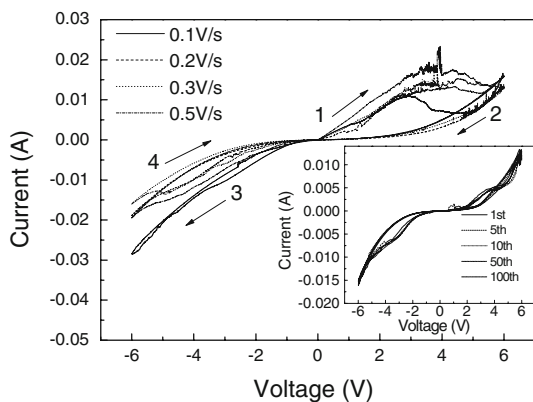

Fig. 3 I–V characteristics of Au/NBT/FTO sandwich structure for resistance switching with different scanning rates. *Inset*: 100 consecutive measurements were performed with a 0.05 V/s scanning rate at room temperature
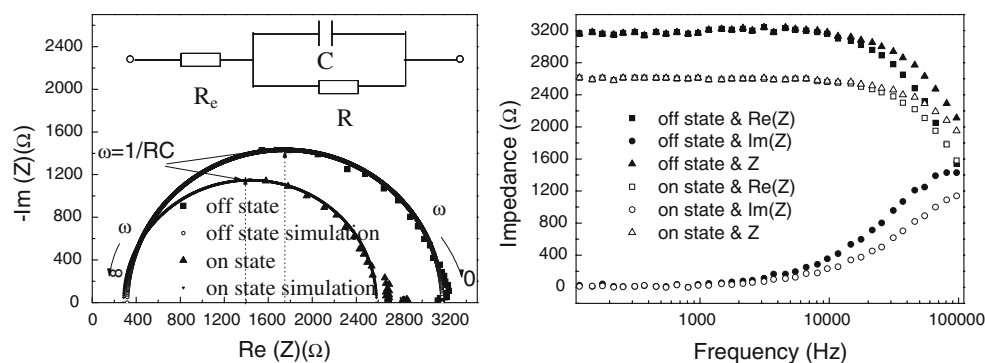
Fig. 4 a Impedance spectra of the NBT memory device are represented by dashed lines. Impedance spectra simulated are represented by *solid lines,* and the corresponding equivalent circuit models are shown in the insert. **b** Frequency dependence of the impedance spectra in the on state and off state. *Solid* symbols correspond to the high-resistance states and *open* symbols correspond to low-resistance states

$$O_O \Leftrightarrow V_O + 1/2O_2, \tag{3}$$

$$V_O \Leftrightarrow V_{\dot{O}} + e', \tag{4}$$

$$V_{\dot{O}} \Leftrightarrow V_{\ddot{O}} + e', \tag{5}$$

or these electrons might be bonded to Ti^{4+} in the form of

$$Ti^{4+} + e' \Leftrightarrow Ti^{3+}. \tag{6}$$

Here, the notation defined by Kröger and Vink is adopted; $V_{\dot{O}}$ and $V_{\ddot{O}}$ represent the oxygen vacancies carrying one and two positive charges, respectively [17]. In the oxygen depletion layer, plenty of oxygen vacancies are positively charged and, hence, act as donor-type native defects, increasing the resistance of the interface region because of the compensation effect.

The simulant plots of on and off electronic states in Fig. 4a could be expressed by

$$Z_j^2 + (Z_i - R_e - 1/2R)^2 = (1/2R)^2 \tag{7}$$

The characteristic impedance is identical to that given in Eqs. 1, 2. Detailed circuit parameters are summarized in Table 1. Because the high-frequency range corresponds to the resistance from the bulk portion [18], this is similar to the scale of resistance obtained with DC *I–V* measurements. The change of bulk-related R_e is not visible, while R represented the charge transfer at the electrode–semiconductor interface changes remarkably. It indicates a significantly changed interface resistance existing in different electronic states. In addition, the switching behavior could be explained in terms of the interfacial response originating from the Au/NBT contacts, since the nonOhmic effects lead to much capacitance, e.g., in the range of nanofarads [19].

One significant disadvantage of the complex-impedance-plane format is that the frequency dependence is obscured. The following frequency-dependent impedance investigation was then used to trace the dynamic process of

Table 1 Summary of the equivalent circuit parameters obtained using impedance spectra of Fig. 3a at the on and off states

	Off state	On state
R_e/Ω	285	311
$C/\times 10^{-10}F$	8.889	8.816
R/Ω	2843	2091

Source by Ting Zhang et al.

the electron charge and mass transport in particular at the interface of on and off states. Frequency is generally presented on a logarithmic scale to reveal the important behavior seen at lower frequencies. Therefore, the impedance associated with frequency plots are depicted in Fig. 4b. The measured impedance is expected to be ω dependent. Interestingly, the impedance information obtained during the off state was similar to that of on state. The bias sweeping showed a gradual decrease in impedance unlike the rapid changes in the current–voltage characteristics. Once the device is in the high impedance state, it can switch to higher conductive states by applying different frequency, which is considered to be a precursor sign of the multilevel resistance switching.

Up to date, similar interface-related electrical characteristics have been observed in many studies. Sawa et al. [20] believed that the resistance switching only occurs at $Ti/Pr_{0.7}Ca_{0.3}MnO_3$ interface after investigating the effects of several top electrodes such as SRO, Pt, Au, Ag, and Ti on the resistance switching. Oka et al. [21] proposed a unique mechanism with the first-order interface metal-insulator transition. Markus Janousch et al. [22] pointed out that the microscopic origin of resistance switching in transition-metal-oxide-based memory is an oxygen-vacancy drift occurring in close proximity to one of the electrodes. Due to dense interface defects act as trap centers of carriers exist at the Au/NBT interface, it is important to understand the basic electric-pulse-induced resistance (EPIR) principles. It

has been concluded by Chen Ang et al. [23] that the oxygen vacancies lead to shallow-level electrons, which may be trapped by Ti^{4+} ions or oxygen vacancies and are easy to be activated by conducting electrons. It has been proposed that the ionizations of oxygen vacancies are responsible for the conduction in the low- and high-resistance states [17]. In their work, at room temperature, the obtained activation energy corresponding to the first ionization of oxygen vacancies of 0.093 eV is responsible for the low-resistance states, while at high-resistance state, the conducting electrons are dominated by the second ionization of oxygen vacancies with the activation energy of 0.63 eV. In perovskite oxides, the activation energy of the first ionization of oxygen vacancies as expressed in Eq. 4 was reported to be 0.1 eV [23–25] and the second ionization of oxygen vacancies [as described in Eq. 5] to the conduction band, the activation energy for conduction was demonstrated to be around 0.7 eV [23, 26]. Both are very near to the activation energy of BSZT films as mentioned in Reference 17. For BNT thin films, the electron trapping accountable for the transition of resistance states can be deduced in the light of the defect formations and the obtained activation energies. At room temperature, the higher E_a for the second ionization of oxygen vacancies compared to that for the first ionization indicates that it is more difficult to activate the conducting electrons without any applied field, and hence, the low free-electron concentration is in agreement with the high-resistance state at which the initial samples were set. $V_{\ddot{O}}$ acts as the carriers in such case and p-like behaviors can be expected [24]. After the samples were set at low-resistance state, according to the first ionization process, the existence of V_O is in accord with the assumption about the electrons trapped by the oxygen vacancies. The activated conducting electrons increase the free electron concentration, representing the n-like conduction. Although detailed investigations on the hysteretic current–voltage characteristics were not performed in our work, it can still be suggested that the first and the second ionization of oxygen vacancies are responsible for the conduction in the low- and high-resistance states, respectively.

In order to evaluate the potential application in nonvolatile memory devices, the retention and endurance tests were performed. Figure 5 demonstrates the retention property of the systems. Over a period of 4×10^4 s, the two states triggered by −2.5 V/1 s and 1 V/1 s pulse remained almost unchanged. The inset of Fig. 5 shows the multilevel resistance switching (MLRS) of Au/NBT/FTO heterostructure. Three resistance states were obtained by applying electric pulses of 2 V/0.002 s, 4 V/0.002 s, and 6 V/0.002 s respectively. This resistance switching feature can be used as the multilevel memory, and the endurance characteristic indicates that the device becomes negligibly degraded. In our experiments, the obtained multilevel resistance states
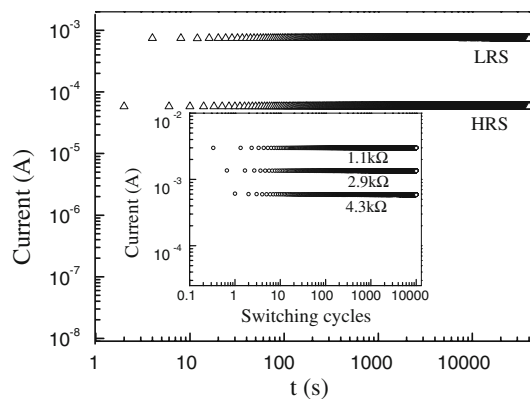

Fig. 5 Plots of retention of the device, and the *inset* shows multilevel switching behavior measurement at the ambient temperature

may be attributed to the trap partial filling in the Au/NBT/FTO structure by applying electric pulses with different voltages. These results indicate that NBT RRAM is highly promising as a future nonvolatile memory device.

Conclusions

In summary, we demonstrated the reproducible resistance switching of an Au/NBT/FTO sandwich system by sol–gel process with an electrochemical workstation. An interfacial resistance switch was found in metal/NBT systems. The charge and mass transfer may occur at this interface due to the local solid electrochemical reaction. We propose that, at room temperature, the first ionization of oxygen vacancies is responsible for the conduction of low-resistance state, while at high-resistance state, the conducting electrons at room temperature are dominated by the second ionization of oxygen vacancies. Several resistance states were obtained by modulating the electric-pulse voltage. It is expected that the resistance switching behavior observed in this work can make it possible to integrate the nonvolatile multilevel memory device on glass substrates.

References

1. S. Kim, Y.K. Choi, Appl. Phys. Lett. **92**, 223508 (2008)
2. C.B. Lee, B.S. Kang, A. Benayad, M.J. Lee, S.-E. Ahn, K.H. Kim, G. Stefanovich, Y. Park, I.K. Yoo, Appl. Phys. Lett. **93**, 042115 (2008)
3. M. Hasan, R. Dong, H.J. Choi, D.S. Lee, D.J. Seong, M.B. Pyun, H. Hwang, Appl. Phys. Lett. **93**, 052908 (2008)

4. T. Zhang, Z.H. Su, H.J. Chen, L.H. Ding, W.F. Zhang, Appl. Phys. Lett. **93**, 172104 (2008)

5. H. Kohlstedt, A. Petraru, K. Szot, A. Rüdiger, P. Meuffels, H. Haselier, R. Waser, V. Nagarajan, Appl. Phys. Lett. **92**, 062907 (2008)

6. Y.D. Xia, W.Y. He, L. Chen, X.K. Meng, Z.G. Liu, Appl. Phys. Lett. **90**, 022907 (2007)

7. K. Tsubouchi, I. Ohkubo, H. Kumigashira, M. Oshima, Y. Matsumoto, K. Itaka, T. Ohnishi, M. Lippmaa, H. Koinuma, Adv. Mater. **19**, 1711 (2007)

8. R. Waser, M. Aono, Nat. Mater. **6**, 833 (2007)

9. A. Sawa, Mater. Today **11**, 28 (2008)

10. S.H. Chang, J.S. Lee, S.C. Chae, S.B. Lee, C. Liu, B. Kahng, D.-W. Kim, T.W. Noh, Phys. Rev. Lett. **102**, 026801 (2009)

11. G.A. Smolenskii, V.A. Isupov, A.I. Agranovskaya, N.N. Krainik, Sov. Phys-Solid State **2**, 2651 (1961)

12. Z.H. Zhou, J.M. Xue, W.Z. Li, J. Wang, H. Zhu, J.M. Miao, Appl. Phys. Lett. **85**, 804 (2004)

13. M.J. Rozenberg, I.H. Inoue, M.J. Sánchez, Appl. Phys. Lett. **88**, 033510 (2006)

14. K. Shono, H. Kawano, T. Yokota, M. Gomi, Appl. Phys. Expr. **1**, 055002 (2008)

15. S. Tsui, Y.Q. Wang, Y.Y. Xue, C.W. Chu, Appl. Phys. Lett. **89**, 123502 (2006)

16. M.E. Orazem, B. Tribollet, *Electrochemical Impedance Spectroscopy* (Wiley, Hoboken, New Jersey, 2008) (sponsored by the Electrochemical Society)

17. Y.D. Xia, Z.G. Liu, Y. Wang, L. Shi, L. Chen, J. Yin, X.K. Meng, Appl. Phys. Lett. **91**, 102904 (2007)

18. C.H. Liang, K. Terabe, T. Hasegawa, M. Aono, Nanotechnology **18**, 485202 (2007)

19. Y.H. You, B.S. So, J.H. Hwang, W. Cho, S.S. Lee, T.M. Chung, C.G. Kim, K.S. An, Appl. Phys. Lett. **89**, 222105 (2006)

20. A. Sawa, T. Fujii, M. Kawasaki, Y. Tokura, Appl. Phys. Lett. **85**, 4073 (2004)

21. T. Oka, N. Nagaosa, Phys. Rev. Lett. **95**, 266403 (2005)

22. M. Janousch, G.I. Meijer, U. Staub, B. Delley, S.F. Karg, B.P. Andreasson, Adv. Mater. **19**, 2232 (2007)

23. C. Ang, Z. Yu, L.E. Cross, Phys. Rev. B **62**, 228 (2000)

24. C.C. Wang, L.W. Zhang, Phys. Rev. B **74**, 024106 (2006)

25. J. Daniels, K.H. Hardtl, Philips Res. Rep. **31**, 480 (1976)

26. K. Morii, H. Kawano, I. Fujii, T. Matsui, Y. Nakayama, J. Appl. Phys. **78**, 1914 (1995)